



# Warm deep drawing behavior of Inconel 625 alloy using constitutive modelling and anisotropic yield criteria

Nitin Kotkunde<sup>1</sup> · Anand Badrishi<sup>1</sup> · Ayush Morchhale<sup>1</sup> · Prathamesh Takalkar<sup>1</sup> · Swadesh Kumar Singh<sup>2</sup>

Received: 13 June 2019 / Accepted: 12 August 2019 / Published online: 29 August 2019  
© Springer-Verlag France SAS, part of Springer Nature 2019

## Abstract

The present work provides a systematic approach to investigate anisotropic yield criteria and constitutive modeling and its applicability in finite element analysis of warm deep drawing behavior of Inconel 625 alloy. Firstly, the material properties and flow stress behavior of Inconel 625 alloy have been determined at temperatures (room temperature (RT) to 400 °C at an interval of 100 °C) at (0.0001–0.1 s<sup>-1</sup>) strain rates using uniaxial tensile tests. The flow stress behavior is influenced significantly by strain rate and temperature variation. Various mechanical properties and anisotropic parameters have been studied at different strain rates and temperatures. On the basis of flow stress data, Sellers constitutive model with different anisotropic yield criteria namely; Hill'48 and Barlat'89 has been developed. Subsequently, experiments of deep drawing have been conducted at various processing conditions. The process parameters effect on Limiting Draw Ratio (LDR), thickness distribution, Maximum Thinning Rate (MTR) and Thickness Deviation (TD) has been investigated. Furthermore, Sellers constitutive model coupled with anisotropic yield criteria has been implemented in ABAQUS software using UMAT subroutine. Sellers model coupled with Barlat'89 yield criterion displayed an accurate prediction of warm deep drawing behavior.

**Keywords** Inconel 625 alloy · Material properties · Warm deep drawing · Constitutive model · Anisotropic yield criteria · Finite element analysis

## Introduction

Inconel 625 is a high strength nickel chromium superalloy. It has various other definitive properties such as resistance to corrosion, creep, fatigue and oxidation up to considerably high temperatures [1, 2]. It has numerous applications in petrochemical, aerospace, marine and nuclear industries because of its corrosion resistance and high strength properties at elevated temperatures [3]. Sheet metal forming is a primary process used in many manufacturing industries because of its cost-effective alternative solution for traditional machining and welding for mass production [4]. However, Inconel alloys have various challenges such as, it's forming is difficult at room temperature due to very high strength and limited

workability when compared with different traditional structural alloys such as aluminum and steel [5]. One of the proven ways to overcome such difficulty is warm or hot forming. Warm forming is usually done to provide easy drawability to the high strength metals which usually tend to get fracture at room temperature [6].

The quality of formed product is dependent on many vital process parameters, tool interaction, friction. The complexity is further enhancing at high temperatures [7]. Moreover, with increase in demand of complex components, the costly high strength material, tooling cost, labour cost etc. are driving sheet metal industries to use accurate and trustworthy Finite Element (FE) analysis tool to predict deformation and forming behaviour [8, 9]. Recently, extensive works have been reported about the thermo-mechanical FE simulations for hot working processes [6]. These FE tools are having highly accurate prediction ability, less time consuming and effectively reduced the costly try-outs of tool and die [10]. However, an effective and accurate utilisation of these software is a big challenge which essentially require many prerequisites such as accurate input material properties, appropriate material model selection and its implementation in FE software. As commercially

✉ Nitin Kotkunde  
nitink@hyderabad.bits-pilani.ac.in

<sup>1</sup> Mechanical Engineering Department, BITS Pilani, Hyderabad Campus, Hyderabad, Telangana, India

<sup>2</sup> Mechanical Engineering Department, GRIET, Hyderabad, Telangana, India

available FE software is generic in nature and do not offer highly specialized material models which can handle complex forming simulations. The situation becomes more complex for high strength, high temperature forming process [11, 12].

An accurate prediction of material behaviour requires suitable selection of constitutive model and anisotropic yield criteria in FE simulations. Constitutive modelling helps in describing an accurate stress strain relationship at several considered processing conditions such as strain rates, temperature and strain [13]. In literature, extensive work has been reported about the development of physical and phenomenological based constitutive models for different class of materials [14]. Recently, few efforts have been made for constitutive model development of nickel based super alloys [15, 16]. Many recent articles mentioned that Arrhenius based phenomenological constitutive model was more suitably used for nickel-based alloy [17].

It is a well-known fact that traditional von-Mises and Tresca yield criteria is not suitable for sheet metal forming applications because of anisotropic behaviour of a material. Several efforts were made in past to develop anisotropic yield criteria which covers normal and planar anisotropic of a material [18]. Particularly, Hill'48 which is considered to be an addition of plastic anisotropy to von-Mises isotropic criteria is the most popular one for the numerical simulations because of ease to determine material parameters using uniaxial tests [19]. Further, Barlat proposed another yield criterion which constants can be easily determined using uniaxial yield stress values and anisotropic coefficients. Over the years, many other yield criteria are proposed which required multiple tests which covers uniaxial and biaxial loading conditions and its parameter identifications [20]. Generally, the capability of the yield criteria is evaluated based on the yield loci, yield stress and anisotropic coefficient variation with respect of different direction of sheet. The complexity of prediction is enhancing in case of high temperatures due to a stress asymmetry and Bauschinger effect [21]. Recently for Ni-base super alloy, yield stress model was developed based on dislocation theory [22]. However, very limited literature is available on anisotropic yield criteria for high strength nickel based super alloys.

Finite Element simulations are very much helpful in terms of reducing the expensive experimental trials and fixing the process parameters in forming process [23]. The study of mesh convergence was suggested by some researchers in order to predict thickness distribution, failure modes (fracture and wrinkle) and most importantly the size of blank [24]. The drawability of material was validated using FE package by comparing the results of fracture locations, wrinkling pattern, percentage increase in drawn height, thickness distribution and LDR [25]. Extensive work was carried out in thermo-mechanical FE simulation by incorporating various material models for steel and Al. alloys. The subroutine for user defined material (UMAT) had been implemented in past with FE packages in order to solve these material models [26]. However, very few reports were found related

to FE simulation of Inconel alloy at room temperature condition [27].

Thus, present work aims to develop a systematic approach for material testing, constitutive model and anisotropic yield criteria development and its incorporation in FE simulation of warm deep drawing process of Inconel 625 alloy.

## Materials and methods

### Tensile testing

Inconel 625 alloy of 0.9 mm sheet thickness is used for experimentation. The chemical composition of alloy is mentioned in Table 1. Molybdenum and chromium are mainly responsible for both the high strength and the corrosion resistance. Niobium is responsible for improvement in the creep strength. The presence of titanium and aluminium causes age hardening, due to precipitation of  $\text{Ni}_3(\text{Al,Ti}) \gamma''$  phase and inhibit creep and slip at elevated temperature [1]. The specimens of tensile test were prepared as per sub sized ASTM E08/E8M-11 standard. The samples at different orientations of sheet viz., Rolling Direction (RD), 45° to RD (ND) and 90° to RD i.e. transverse direction (TD) were prepared as shown in Fig. 1. Computer controlled Zwick/Roell Universal Testing Machine (UTM) as shown in Figs. 2 was used in conducting high temperature tensile test. It has max. Loading capacity of 100 kN with box furnace and non-contact type laser extensometer. The experiments were done from RT to 400 °C at a difference of 100 °C, strain rate (0.1, 0.01, 0.001 and 0.0001 s<sup>-1</sup>) and sheet orientations (RD, ND and TD). The specimens were heated at 20 °C/min followed by holding time of 5 min. The true stress vs. strain data was captured and used for further analysis. For each setting, three samples were tested and average values were reported. The optical micrographs of asreceived Inconel 625 alloy sheet were taken at different sheet orientations. The average ASTM grain size number is 9 with a difference in morphology in RD, ND and TD direction as shown in Fig. 3. The specimen is oriented mostly with fine elongated and compressed grain size in ND and TD directional planes.

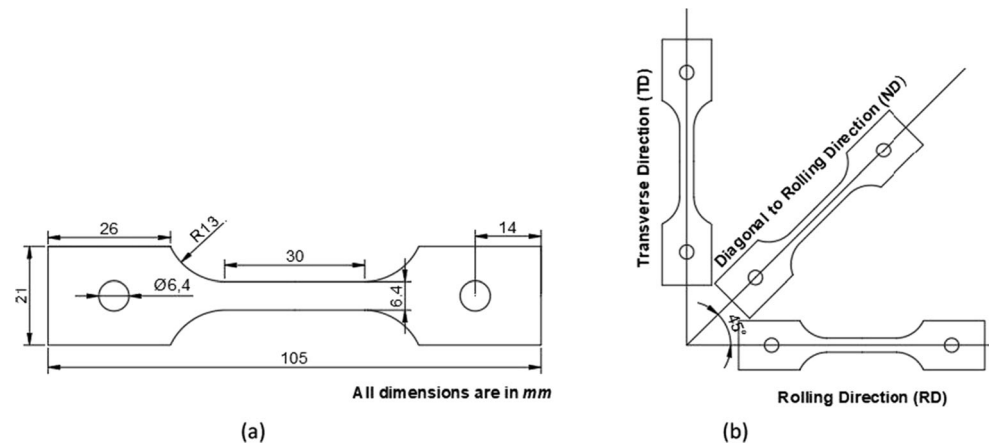
### Deep drawing

The automatic computer controlled hydraulic press setup having maximum capacity of 40 tons as shown in Fig. 4 was used for deep drawing operation. The induction heating setup arrangement

**Table 1** Chemical composition of as received Inconel 625 alloy sheet (wt.%)

Element	Ni	Cr	Nb	Mo	Ti	Al	Fe
wt.%	61.495	21.739	3.271	9.479	0.166	0.067	3.304
Element	C	Si	Mn	P	S	Co	Cu
wt.%	0.021	0.101	0.123	0.001	0.002	0.080	balance

**Fig. 1** Schematic tensile test specimen (a) sub sized ASTM E08/E8M-11 standard (b) with different orientations of a sheet



was used to heat the die at required temperatures. A water cooling was used to control and maintain the desired temperature during the operation. The K-type optical cable probe and PID temperature controller was used to measure the temperature of die at three different locations. The graphene-based moly-spray was used as a lubricant for deep drawing [28]. The CAD model with all the dimensions of deep drawing setup is mentioned in Fig. 5.

Initially, few trials were made in order to fix the process parameters. Severe wrinkling was observed below 15 bar Blank Holding Pressure (BHP) and above 25 bar the resistance in flow of material was very high. Thus, crack was initiated in the beginning of drawing process itself. The cups are drawn with three different punch speed viz. 1.5 and 10 mm/min. The sudden fracture was observed at 12 mm/min punch speed at room temperature condition. This may be because of very high strength and comparatively higher impact of punch on blank leads to fracture in the beginning of drawing stage. Moreover, it was observed that the punch speed has negligible effect on cup height and thickness distribution. Thus, 5 mm/min const. Punch speed was used in all experiments. Finally, deep drawing experiments were performed by varying temperatures and BHP with constant punch speed. The plan of experiments is presented in Table 2. For every setting,

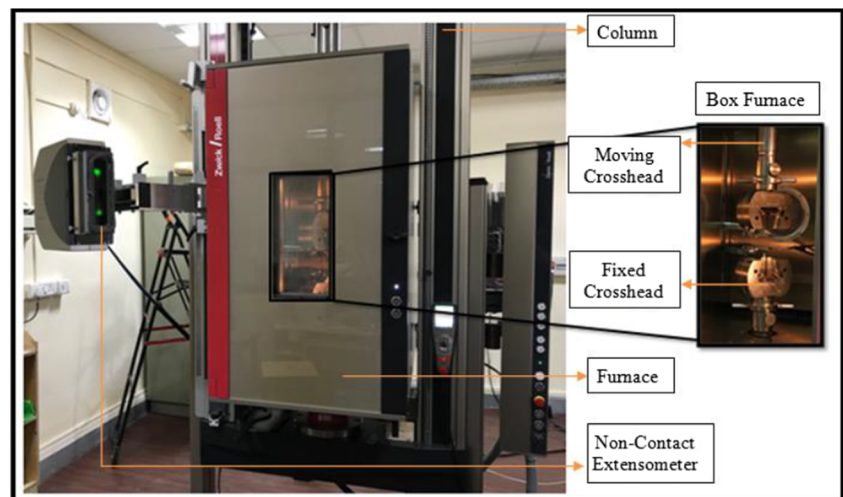
three experiments were performed and average values were considered.

## Results and discussions

### Study of material properties and deformation behaviour

Flow stress representative graphs in rolling direction at strain rates of  $0.01 \text{ s}^{-1}$  &  $0.0001 \text{ s}^{-1}$  are displayed at various considered temperatures in Fig. 6 (a&b). As expected earlier, with increase in strain rate and temperature, the flow stress decreases. It was also observed that with small increase in strain (uptill 0.05), steep rise in flow stress takes place because of uniformity in deformation during initial stage which is mainly due to movement of the dislocations. In metals, uniform deformation is usually the initial stage followed by necking which could be either localized or diffused and finally failure in terms fracture takes place. Flow stress further increases slowly till point of ultimate strength ( $\sigma_{\text{uts}}$ ) of material is achieved.

**Fig. 2** Universal Testing Machine (UTM) of 100 kN capacity with non-contact type laser extensometer



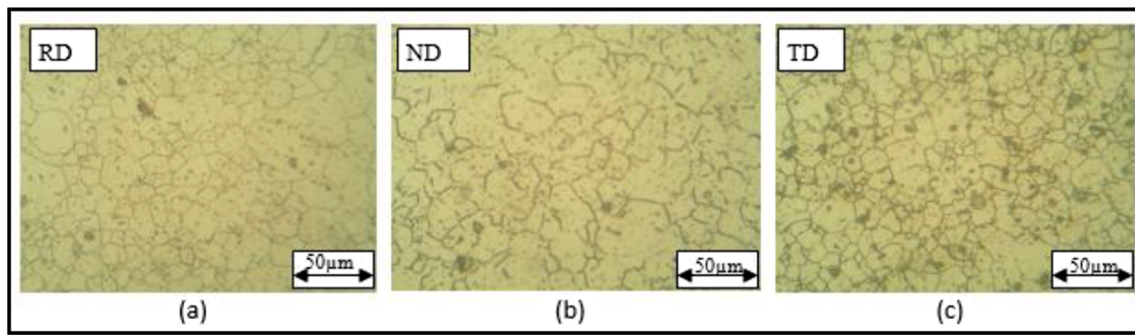


**Fig. 3** Microstructure of as-received Inconel 625 alloy sheet (a) RD (b) ND (c) TD

Representative graphs of flow stress vs. strain at two extreme considered test temperatures for various strain rates are shown in Fig. 7 (a & b). Strain dependence property of material could be observed at RT, as its yield strength decreased to 780 MPa from 851 MPa as strain rate increased from  $0.0001 \text{ s}^{-1}$  to  $0.1 \text{ s}^{-1}$ . Considerable strain hardening is also observed at RT for small strain rates and it decreased with increase in strain rate. During manufacturing of sheet, thermal softening and consequent adiabatic heating might be the possible reason for observed strain hardening behavior. The flow stress behavior varies with the sheet rolling direction and its representative graph at  $0.01 \text{ s}^{-1}$  strain rate with RT and  $400 \text{ }^\circ\text{C}$  as testing temperature is shown in Fig. 8 (a & b). Considerable effect of rolling direction could be observed at  $400 \text{ }^\circ\text{C}$ .

Various mechanical properties are calculated at quasi static strain rate ( $0.001 \text{ s}^{-1}$ ) and different temperatures in 3 different directions (TD, ND & RD) is shown in Table 3. 3 iterations were considered for each experiment and their average values were considered for analysis. As the temperature increased from RT to  $400 \text{ }^\circ\text{C}$ , the yield strength and ultimate strength decreased by approximately 25% and 18% respectively but % elongation increased by approximately 7%. The directionality of any property of material is defined by its anisotropy. Lankford coefficient (R) is used to define the plastic anisotropy along  $0^\circ$ ,  $45^\circ$  &  $90^\circ$  of sheet orientation [29].

### Warm deep drawing experiments

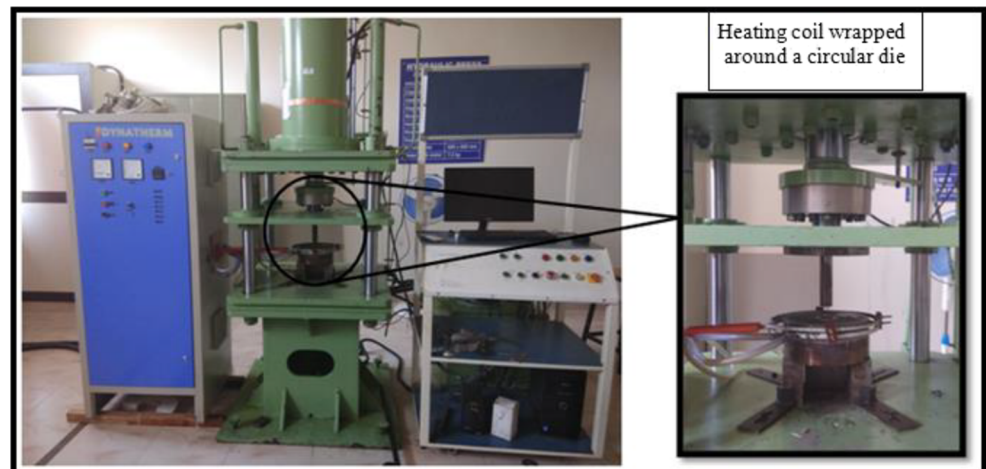
In case of deep drawn components, thinning is the main cause of failure. Usually, the side walls of deep drawn cup are undergoing severe thinning while the flange and center area of cup have almost evenly distributed thickness. In hot deep drawing, the metallic part which is near to punch shows rapid downfall in its temperature. The metal part of cup, which is not in contact with punch, like sidewalls, shows gradual decrease in temperature. The hot part gets deformed as it is the soft in nature while the cold part remains hardened resulting in replacement of overall local deformation. Therefore, the thinning rate in deep drawn cup is maximum near the punch nose radius and least in top of the wall. The more uniformity in overall thickness and maximum thinning rate is considered as a basis for good quality of drawn cup [30]. The calculation of considered characteristics is done based on Eqs. (1) and (2).

$$\text{MTR} = ((y_{\text{ini}} - y_{\text{min}}) / y_{\text{ini}}) \times 100 \quad (1)$$

$$\text{TD} = \frac{1}{n-1} \sum_{i=1}^n (y_i - \bar{y})^2 \quad (2)$$

where MTR is maximum thinning rate, TD is thickness deviation,  $y_{\text{min}}$  is minimum thickness,  $y_{\text{ini}}$  is initial thickness and  $y_i$  is thickness at any point  $i$  and  $n$  is total experiments.

**Fig. 4** Hydraulic press setup with magnified view of deep drawing dies and induction heating arrangement





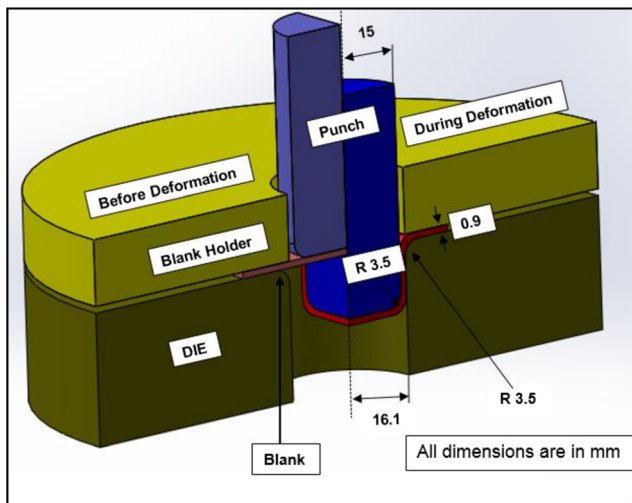


Fig. 5 CAD model of deep drawing setup with all the dimensions

The representative trend about effect of temperature on thickness distribution, MTR and TD at constant BHP of 15 bar and 5 mm/min punch speed is shown in Fig. 9 (a & b). The variation of normalised thickness at distance from centre of cup at different temperatures is displayed in Fig. 9 (b). As expected, the thickness almost remains constant at bottom of cup followed by the minimum thickness or excessive thinning at punch corner region and further the thickness increased till the upper tip of wall of cup. The variation in thickness distribution values are more in wall region for lower temperature case and comparatively less at higher temperature. The possible reason is, may be at higher temperature the material becomes more flowable with increase in ductility. Therefore, resistance to deformation is less during the drawing process which facilitate the more uniform thickness distribution in cup of wall. The similar trend is found in case of MTR. The MTR percentage is high in case of RT and subsequently reduces as temperature increases. However, as temperature increases, the variation in TD is also increasing. Precisely, the temperature is having significant effect on thickness distribution of deep drawn cups.

The representative trend of significance of BHP on MTR and TD, thickness distribution at Room Temperature (RT) and 5 mm/min Punch Speed is shown in Fig. 10 (a& b). Excessive thinning is observed at higher BHP. The possible reason may be higher BHP resist easy flow of metal during deep drawing process which increases the friction in between die corner region and punch. Similar observations are found for MTR and TD. The MTR and TD increase significantly at higher BHP. Thus, lower BHP provides more uniform thickness distribution.

Table 2 Process parameters for deep drawing analysis

Temperature (°C)	RT			100			200			300			400		
BHP (bar)	15	20	25	15	20	25	15	20	25	15	20	25	15	20	25
Experiment No.	1	2	3	4	5	6	7	8	9	10	11	12	13	14	15

The variation of Limiting Draw Ratio (LDR) and percentage increase in height with different temperatures at 15 bar BHP and 5 mm/min punch speed is shown in Fig. 11. Commonly, LDR is calculated based on ratio of initial blank diameter to the punch diameter. As expected, LDR and percentage increase in height of drawn cup increases with temperature as the material become soft at higher temperature and as a result the drawability of material also increases. LDR at room temperature is found as 1.8 which is substantially lower than the other traditional alloy. This signifies the limited drawability of an Inconel 625 alloy at room temperature condition. LDR is increased to 2.13 at 400 °C.

Constitutive modeling

The activation energy is considered as an important parameter to explain the extent of difficulty in the deformation processes at the elevated temperatures. It also acts as a guide for optimizing the process parameters and presents the important information related to changes in microstructure and flow stress at the time of deformation [16]. In this work, Sellers model which is based on activation energy concept is used for flow stress behaviour study for Inconel 625 alloy. The equations which exhibit the relation between strain rates, temperature, flow stresses and activation energy are given in Eq. (3, 4 & 5).

$$\dot{\epsilon} = A_1 \sigma^{n_1} \exp\left(\frac{-Q}{RT}\right) \tag{3}$$

$$\dot{\epsilon} = A_2 \exp(\beta \sigma) \exp\left(\frac{-Q}{RT}\right) \tag{4}$$

$$\dot{\epsilon} = A [\sinh(\alpha \sigma)]^n \exp\left(\frac{-Q}{RT}\right) \tag{5}$$

where,  $A_1, A_2$  are proportionality constants,  $A$  is the structural factor,  $n_1$  is the inverse of strain rate sensitivity,  $n$  is stress exponent,  $\alpha$  and  $\beta$  are stress multipliers,  $\dot{\epsilon}$  ( $s^{-1}$ ) is strain rate,  $\sigma$  (MPa) is true stress,  $T$  is the absolute temperature in Kelvin,  $R$  is the universal gas constant (8.314 J/mol-K) and  $Q$  (kJ/mol) is the hot deformation activation energy. The parameter  $\alpha$  is given by

$$\alpha = \frac{\beta}{n_1} \tag{6}$$

The power law model shown in Eq. 3 best describes the flow behaviour in the low flow stress region ( $\alpha \sigma < 0.8$ ). And the exponential law gives good results in the high flow stress region ( $\alpha \sigma > 1.2$ ). Therefore, the power law and the

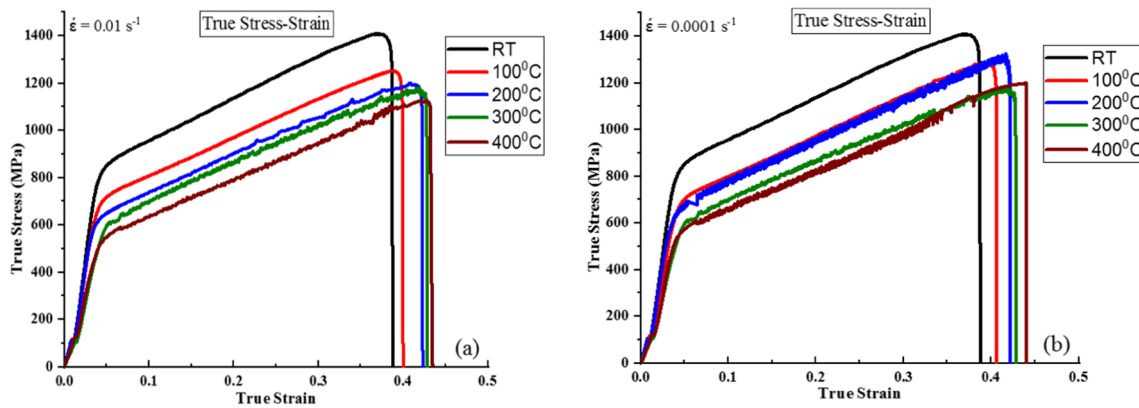


Fig. 6 Representative graphs of true stress-strain at (a)  $0.01 \text{ s}^{-1}$  & (b)  $0.0001 \text{ s}^{-1}$  strain rates for different temperatures

exponential law by themselves are not capable of predicting the flow behaviour over the complete range of flow stresses. These shortcomings led to the development of the hyperbolic sine law, popularly known as the Sellers model as shown in Eq. 5. The Sellers model effectively describes the flow behaviour over the complete flow stress regime [17].

Taking natural logarithm on the both sides of Eq. (3) and Eq. (4), we get

$$\ln \dot{\epsilon} = n_1 \ln \sigma + \ln A_1 - \frac{Q}{RT} \tag{7}$$

$$\ln \dot{\epsilon} = \beta \sigma + \ln A_2 - \frac{Q}{RT} \tag{8}$$

The parameter  $n_1$  was obtained from the mean of the slopes of the linear plot between  $\ln \dot{\epsilon}$  vs.  $\ln \sigma$  as shown in Fig. 12 (a). And the parameter  $\beta$  can be calculated from the mean

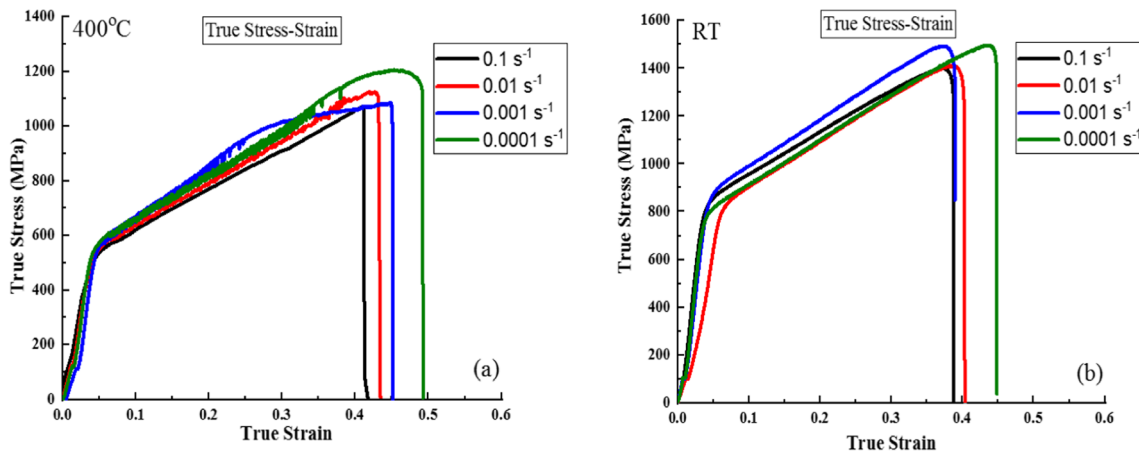


Fig. 7 Representative graphs of true stress vs. true strain at (a)  $400^\circ\text{C}$ , (b) RT with different strain rates

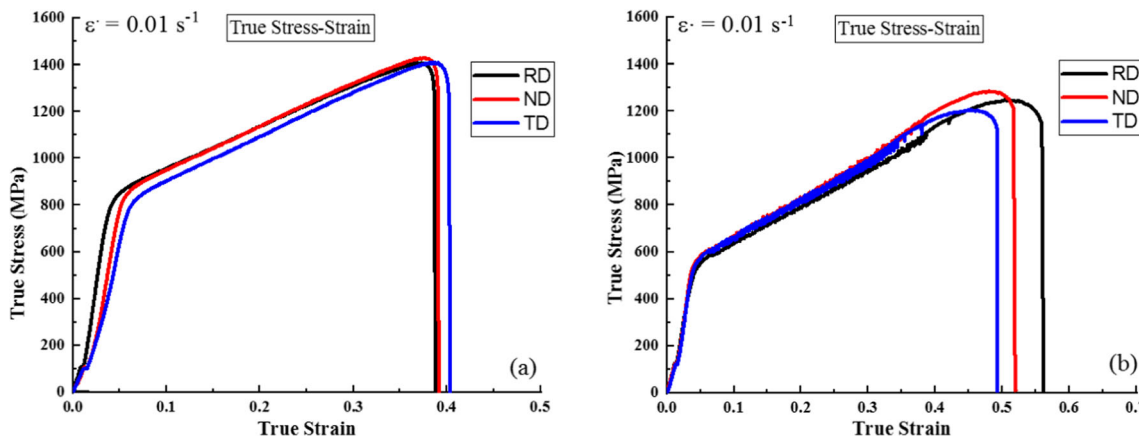


Fig. 8 Representative graphs of true stress vs. true strain at  $0.01 \text{ s}^{-1}$  and (a) RT, (b)  $400^\circ\text{C}$ , at three different orientations

**Table 3** Averagemechanical properties for Inconel 625 alloy

Temperature (°C)	$\sigma_{ys}$ (MPa)	$\sigma_{uts}$ (MPa)	Percent Elongation (%)	Modulus of Elasticity (E) (GPa)	Strain Hardening Exponent (n)	R <sub>0</sub>	R <sub>45</sub>	R <sub>90</sub>
RT	812.07 ± 8	978.55 ± 9	39.65 ± 0.3	207.5 ± 6	0.306	0.8515	0.9686	0.7490
100	776.81 ± 4	959.46 ± 6	41.20 ± 0.3	204.1 ± 5	0.327	0.4980	0.1948	1.1655
200	691.73 ± 6	852.79 ± 7	42.99 ± 0.4	197.9 ± 7	0.325	0.8256	0.8518	1.3906
300	637.54 ± 5	837.15 ± 5	44.25 ± 0.5	191.7 ± 4	0.356	0.6808	0.7916	1.4011
400	609.50 ± 6	805.18 ± 4	46.57 ± 0.5	185.5 ± 3	0.337	1.0869	0.6612	0.7043

of the slopes of the linear plot between  $\ln \dot{\epsilon}$  vs.  $\sigma$  as shown in Fig. 12 (b). The average values of  $n_1$  and  $\beta$  were determined as  $83.97475 \text{ MPa}^{-1}$  and  $0.081825 \text{ MPa}^{-1}$  respectively. The value of stress multiplier  $\alpha$  is calculated using Eq. 6 is  $0.00097 \text{ MPa}^{-1}$ .

To calculate the parameter n, take natural logarithm on the both sides of the Eq. 5, we get

$$\ln \dot{\epsilon} = n \ln \sinh(\alpha\sigma) + \ln A - \frac{Q}{RT} \tag{9}$$

The mean of the slopes of the linear plot between  $\ln \dot{\epsilon}$  vs.  $\ln \sinh(\alpha\sigma)$  gives value of stress exponent n as shown in Fig. 12 (c). The hot deformation activation energy can be determined by partially differentiating Eq. 5 and rearranging the terms such that activation energy Q is given by

$$Q = R n s \tag{10}$$

$$\text{where, } n = \left. \frac{\partial \ln \dot{\epsilon}}{\partial \ln \sinh(\alpha\sigma)} \right|_T \quad \& \quad s = \left. \frac{\partial \sinh(\alpha\sigma)}{\partial \left(\frac{1000}{T}\right)} \right|_{\dot{\epsilon}}$$

The parameter s in the Eq. 9 is obtained from the mean of the slope of the linear plot between  $\sinh(\alpha\sigma)$  vs.  $\frac{1000}{T}$  as shown

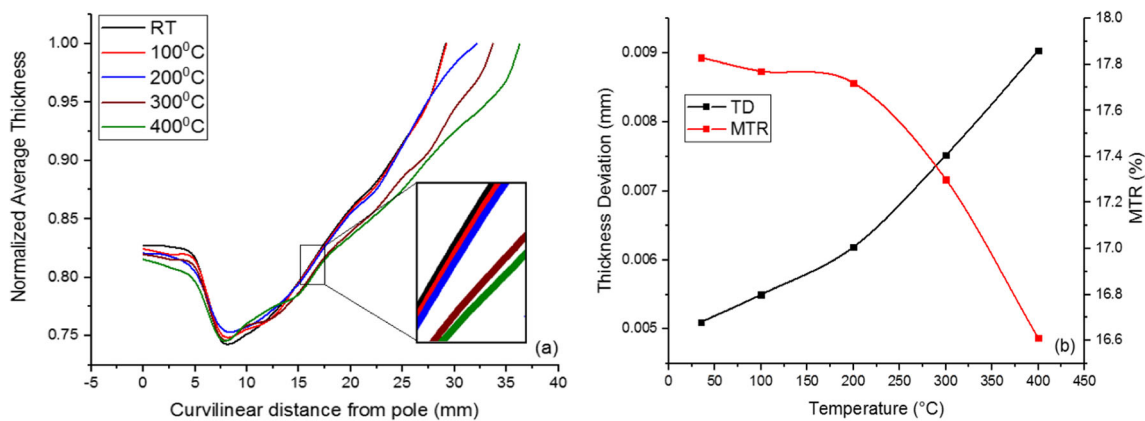


**Fig. 9** Effect of temperature on (a) Normalized Thickness Distribution and (b) MTR & TD

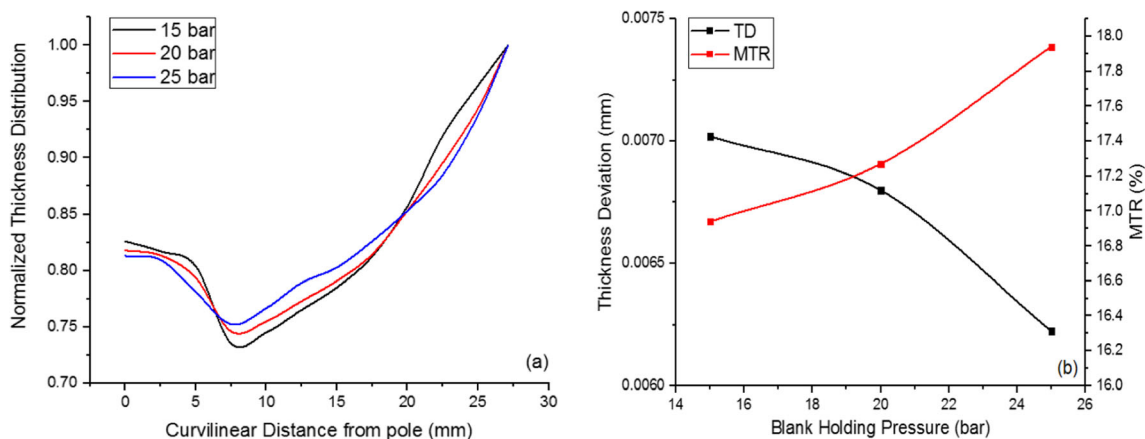


**Fig. 10** Effect of BHP on (a) Normalized Thickness Distribution and (b) MTR & TD

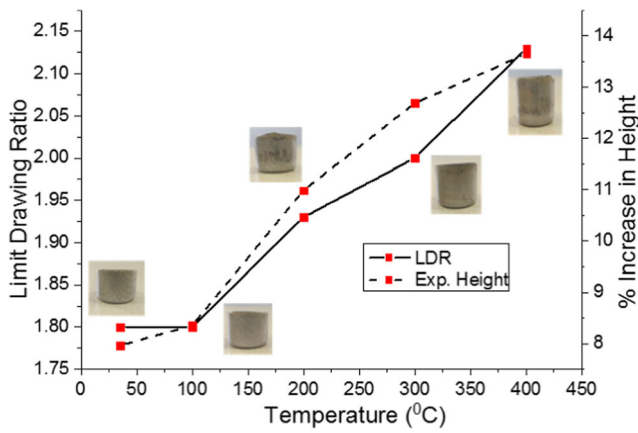


Fig. 11 Variation of LDR and Height with temperature

in Fig. 12 (d). The relation between  $T$  and  $n$  &  $\ln \dot{\epsilon}$  and  $s$  is given in Eq. (10 and 11) and shown in Fig. 13 (a & b) respectively.

$$n(T) = -0.168T + 169.1 \tag{11}$$

$$s(\dot{\epsilon}) = 0.3528 + 0.0687(\ln \dot{\epsilon}) + 0.0062(\ln \dot{\epsilon})^2 \tag{12}$$

Substituting Eq. (11 and 12) into Eq. (9), the combined relation between the temperature ( $T$ ), Strain rate ( $\dot{\epsilon}$ ), and hot deformation activation energy ( $Q$ ) is given by

$$Q(T, \dot{\epsilon}) = 496.0304 - 96.59095(\ln \dot{\epsilon}) + 8.7171(\ln \dot{\epsilon})^2 - 0.49279T - 0.09596T(\ln \dot{\epsilon}) - 0.00866T(\ln \dot{\epsilon})^2 \tag{13}$$

The Eq. (5) can be rearranged to Eq. (14) using the Zener-Holloman parameter ( $Z$ ) in which the temperature term compensates strain rate.

$$Z = A[\ln \sinh(\alpha\sigma)]^n = \dot{\epsilon} \exp(Q/RT) \tag{14}$$

The structural factor  $A$  can be calculated from the intercept of linear plot between  $\ln Z$  vs.  $\ln \sinh(\alpha\sigma)$  as shown in Fig. 14.

The parameters defining the constitutive model are calculated at the at the true strain of 0.2 and are mentioned in Table 4.

Substituting the values of the parameters  $\alpha$ ,  $n$ ,  $Q$  and  $A$  in the Eq. (14) and rearranging the terms, we get constitutive model corresponding to true strain of 0.2

$$\sigma = \left( \frac{1}{0.00097} \right) \text{ArcSinh} \left( \frac{Z}{1.40402} \right)^{\frac{1}{63.885}} \tag{15}$$

where,  $Z = \dot{\epsilon} \exp(12519.39/T)$

Representative comparison of flow stress and strain for predicted and experimental results at  $0.0001 \text{ s}^{-1}$  and  $0.01 \text{ s}^{-1}$  for different temperatures and at RT and  $400 \text{ }^\circ\text{C}$  for different strain rates is shown in Fig. 15 (a, b, c & d) respectively. It was

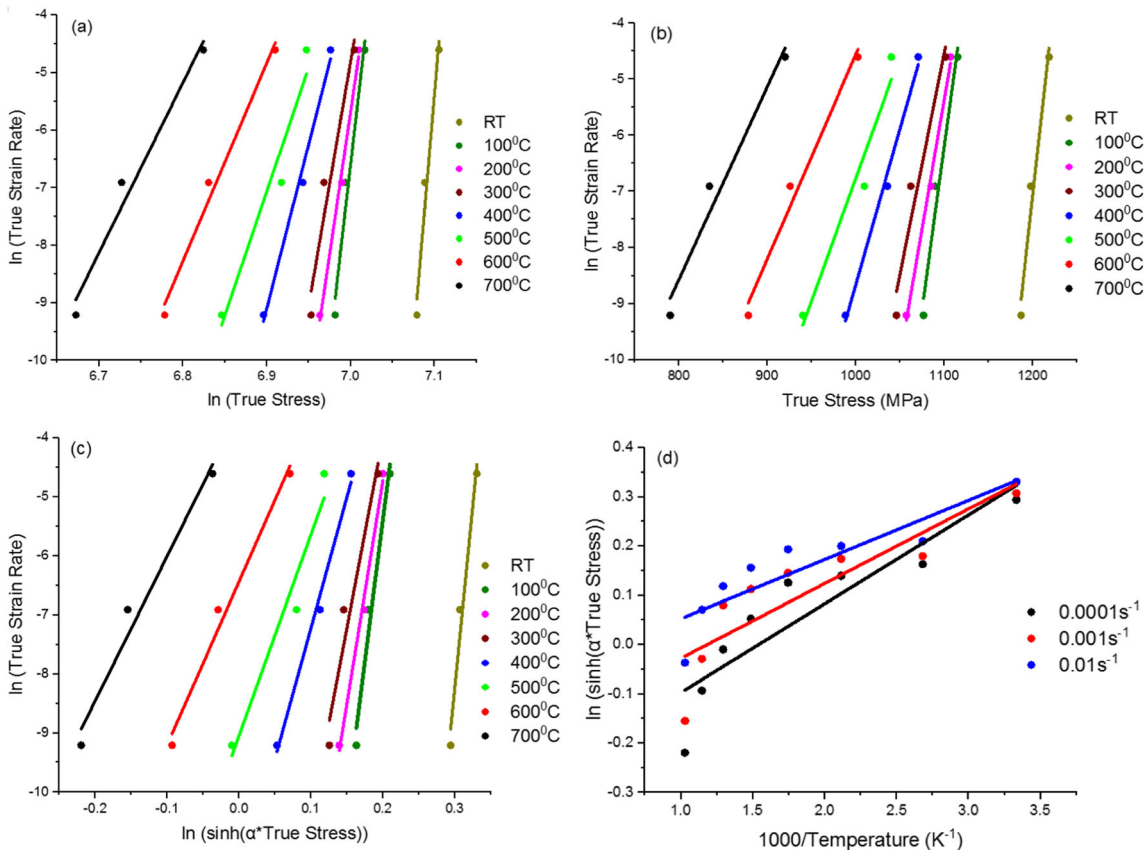


Fig. 12 Plots at 0.2 strain of (a)  $\ln \dot{\epsilon}$  vs.  $\ln \sigma$  (b)  $\ln \dot{\epsilon}$  vs.  $\sigma$  (c)  $\ln \dot{\epsilon}$  vs.  $\ln \sinh(\alpha\sigma)$  and (d)  $\sinh(\alpha\sigma)$  vs.  $\frac{1000}{T}$



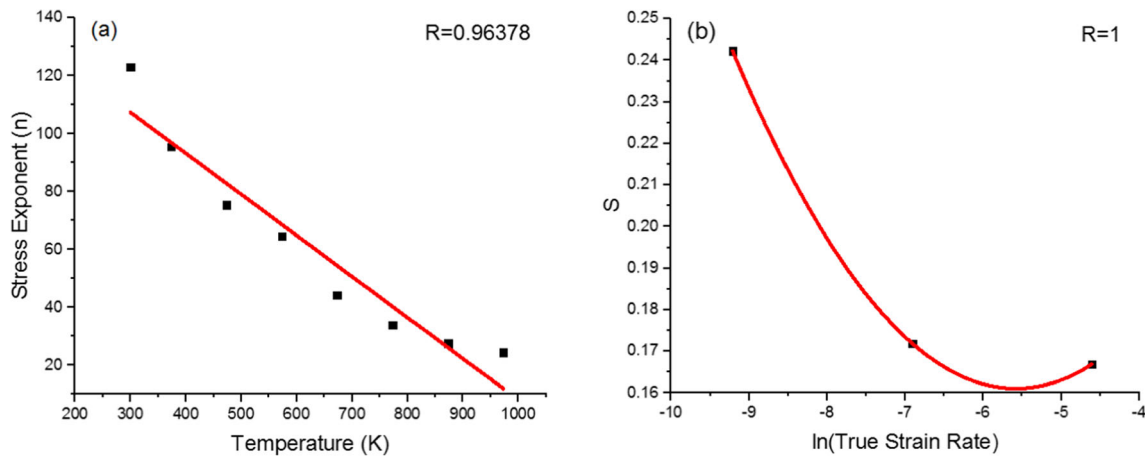


Fig. 13 Plots of (a) T vs. n (b)  $\ln \bar{n}$  vs. s at 0.2 strain

observed the at higher temperature and lower strain rates the predicted flow stress values closely follows the experimental results. The flow stress decreased with decrease in strain rate and increase in temperature.

The activation energy(Q) variation with temperature (T) and Strain rate ( $\epsilon$ ) is given in Fig. 16 (a) and (b) respectively. The activation energy decreases with the increase in both temperature and strain rate. It is known fact the motion of the dislocations is dependent upon the temperature. As the temperature increases, higher number of slip system are activated and consequently there is decrease in dislocation density. Thus, the resistance to the motion of the dislocation is reduced at elevated temperature and hence the activation energy decreased with the increase in the temperature. As the pulling force increases, the strain rate also increases and at the same time the resolved shear stress acting along the slipping direction also increases. This helps in easy motion of various dislocations in crystal structures thus the energy required to overcome energy barrier i.e. activation energy is reduced.

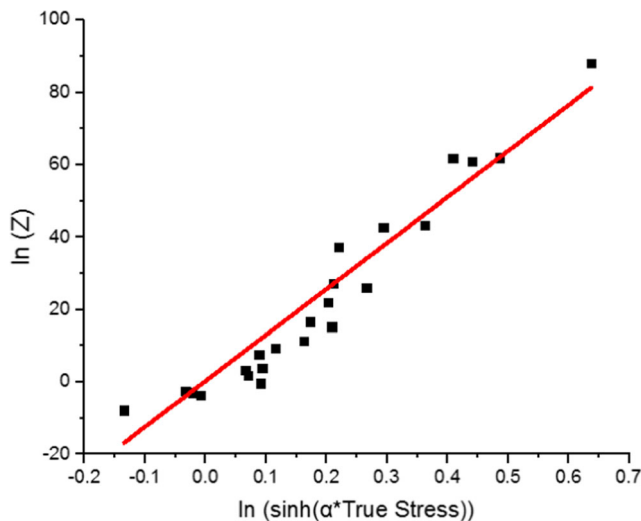


Fig. 14 The plot of  $\ln(Z)$  vs.  $\ln \sinh(\alpha\sigma)$  at 0.2 strain

The accuracy of the developed model is exhibited by using various statistical measures such as standard deviation ( $\delta$ ), avg. absolute percentage error ( $\Delta$ ) and correlation coefficient (R) [5]. The correlation coefficient of predicted vs. experimental flow stress is shown in Fig. 17. The correlation coefficient (R) is found to be 0.9721, standard deviation ( $\delta$ ) is 2.314 and avg. absolute error ( $\Delta$ ) is 5.2616. Based upon the values of the statistical parameters, it can be concluded that the true stress–strain response predicted using Sellers model is found to have a good relation with experimental data.

### Anisotropic yield criteria

The anisotropic yield criteria namely; Barlat’89 and Hill’48 is formulated for Inconel 625 alloy at different strain rates and temperatures. Hill [31] proposed an extension of the von Mises yield function with planar anisotropy. Material yielding response is expressed as elasto-plastic constitutive relationship in terms of yield stress and plastic hardening modulus. The extended yield function is expressed as per Eq. (16).

$$f(\sigma) = \sigma^2 = F\sigma_{22}^2 + G\sigma_{11}^2 + H(\sigma_{11}-\sigma_{22})^2 + 2N\sigma_{12}^2 \quad (16)$$

where, F, G, H and N are anisotropic material coefficients. These material constants can have calculated by two different methods namely r-value based method and  $\sigma$ -value based method. In the present study, material parameters are evaluated based on r-value based method. Barlat [32] developed a plane stress anisotropic yield function. It is expressed as per Eq. (16).

Table 4 Sellers model parameters at true strain of 0.2

$\alpha$ (MPa <sup>-1</sup> )	n	Q (kJ/mol)	A (s <sup>-1</sup> )
0.00097	63.885	104.0925	1.4010

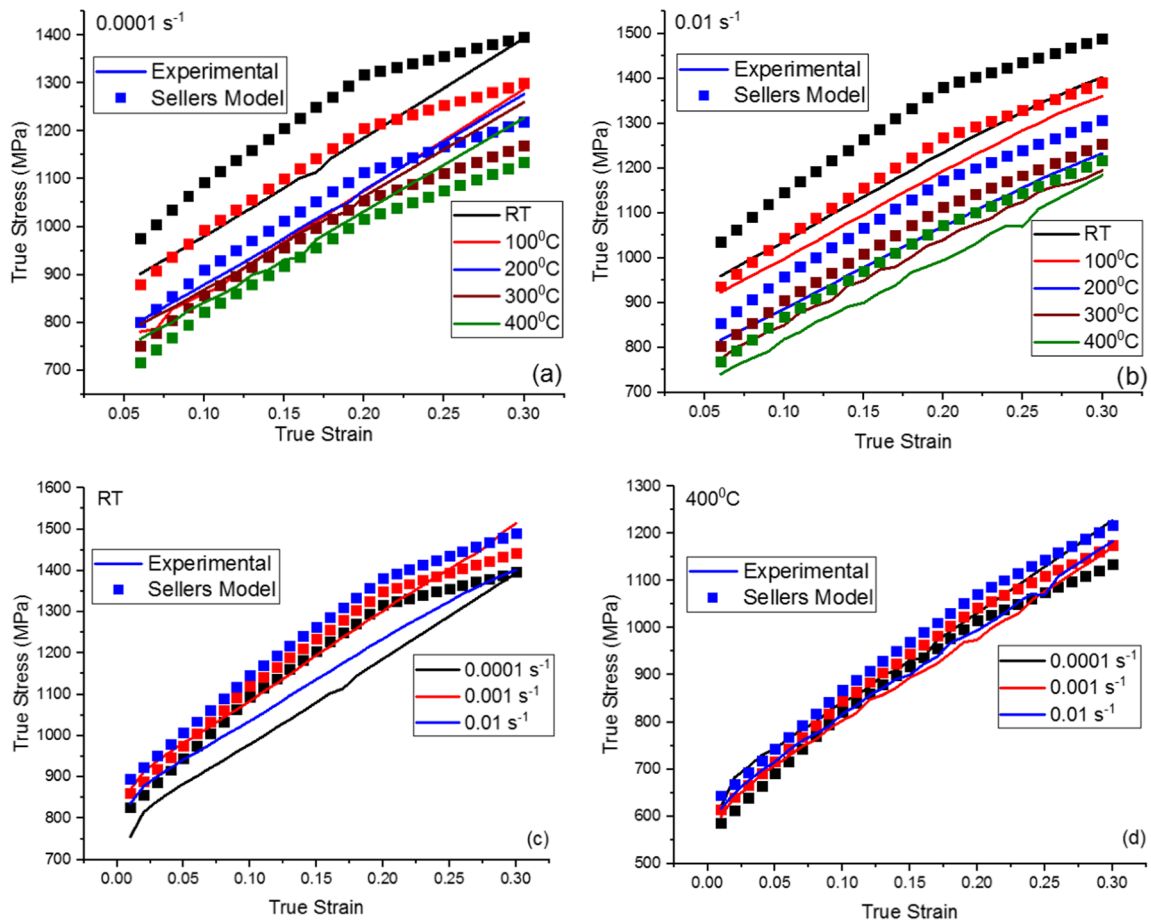


Fig. 15 Plots comparing experimental flow stress and strain at different temperatures for (a) 0.0001 s<sup>-1</sup>, (b) 0.01 s<sup>-1</sup>; at different strain rates for (c) RT, (d) 400 °C

$$2\sigma^m = a|k_1 + k_2|^m + a|k_1 - k_2|^m + c|2k_2|^m = \phi \quad (17)$$

where,  $k_1$  and  $k_2$  is expressed in terms of yield stress as

$$k_1 = \frac{\sigma_1 - h\sigma_2}{2} \quad (18)$$

$$k_2 = \sqrt{\left(\frac{\sigma_1 - h\sigma_2}{2}\right)^2 - p^2\tau_{12}^2} \quad (19)$$

In Eq. (17), (18) and (19), a, c & h are anisotropy ratio functions and expressed as

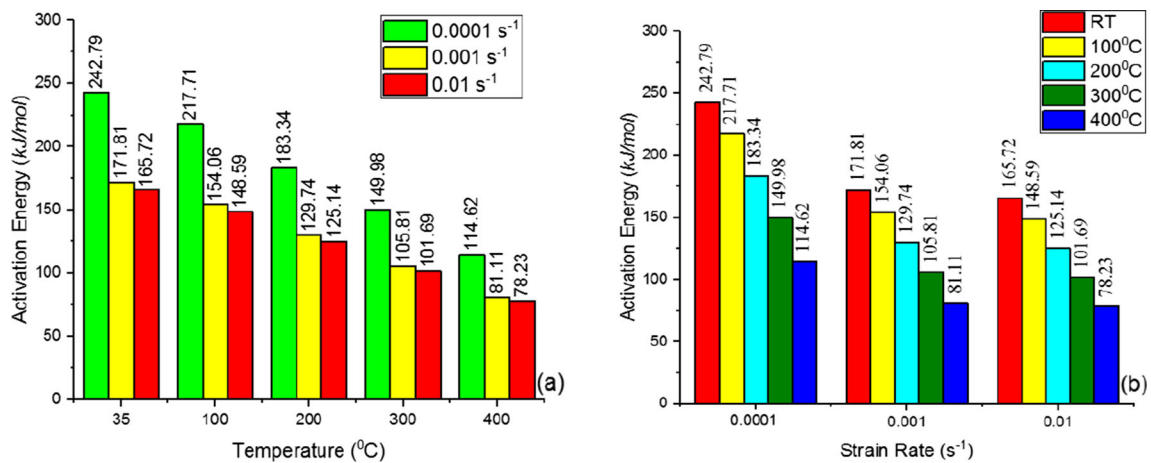
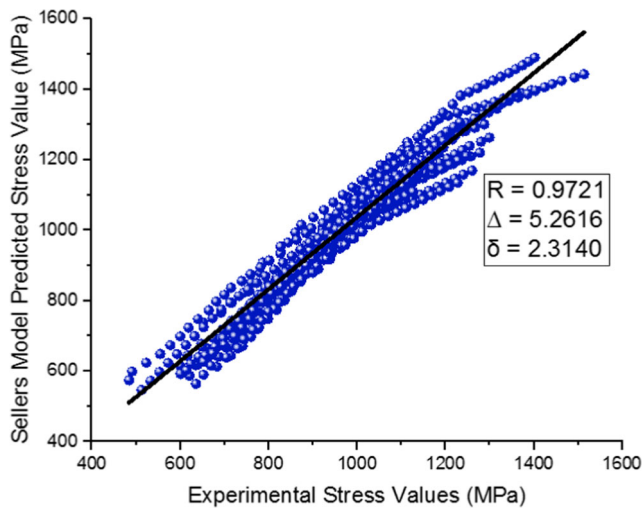


Fig. 16 Variation of activation energy (Q) with (a) Strain rate ( $\dot{\epsilon}$ ) & (b) Temperature (T)



**Fig. 17** Statistical parameters for predicted flow stress using Sellers model

$$a = 2 \left( 1 - \sqrt{\frac{r_0 r_{90}}{(1 + r_0)(1 + r_{90})}} \right) \quad (20)$$

$$h = \sqrt{\frac{r_0(1 + r_{90})}{r_{90}(1 + r_0)}} \quad (21)$$

$$c = (2 - a) \quad (22)$$

Here,  $r_0$  &  $r_{90}$  is anisotropy ratio measured in RD and TD directions of sheet material respectively.  $p$  value is considered iteratively. To find the value of  $p$  value, the variation of Lankford parameter w.r.t. angle  $\theta$  from RD is taken as per Eq. (23).

$$r_\theta = \frac{2m\sigma_0^m}{\sigma_\theta \left( \frac{\partial \phi}{\partial \sigma_{11}} + \frac{\partial \phi}{\partial \sigma_{22}} \right)} - 1 \quad (23)$$

Value of angle  $\theta$  is taken as  $45^\circ$  to relate the  $p$  value and for further iteration. In all above equations,  $m$  is yield function exponent which depends upon crystallography ( $m$ -value is considered as 8 for FCC structure).

The representative comparative yield loci, anisotropic coefficient variation and yield stress variation for Hill'48 and Barlat'89 with experimental results at  $400^\circ\text{C}$  are shown in Fig. 18 (a, b & c). It can be observed from Fig. 18 (a) that the

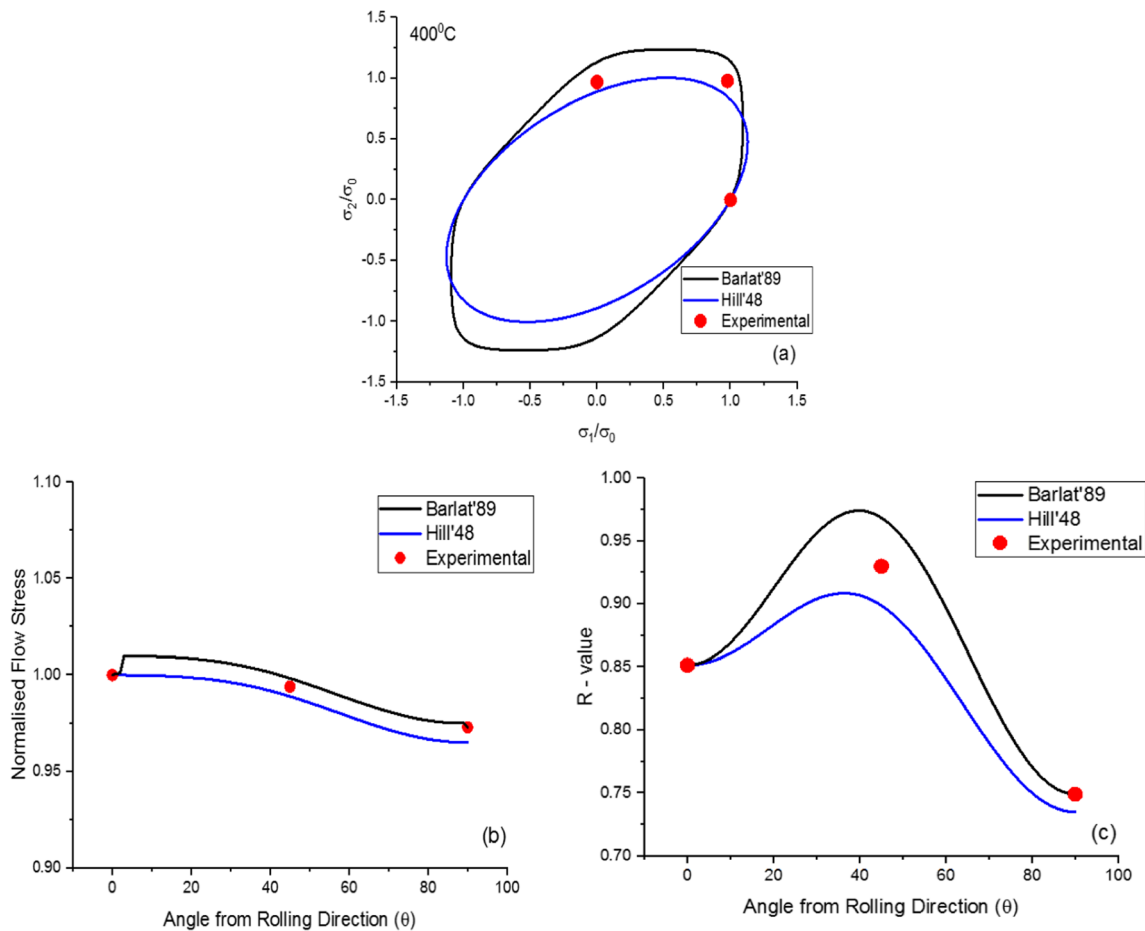


**Fig. 18** Representative comparison of yield criteria at  $400^\circ\text{C}$  and  $0.01\text{ s}^{-1}$  strain rate (a) yield loci, (b) normalized flow stress variation (c) normalized anisotropic coefficient variation

**Table 5** Mesh sensitivity analysis

Mesh Description	Size (mm <sup>2</sup> )	Simulation Results	
		Max. thinning (mm)	CPU run time(sec)
Coarse	5 × 5	0.956	3960
Medium	2.5 × 2.5	0.922	4862
Fine	1.5 × 1.5	0.866	5932
Fine	1 × 1	0.830	6782
Very Fine	0.5 × 0.5	0.796	8235
Ultra Fine	0.25 × 0.25	0.775	10,562

Experimental Maximum Thinning: 0.854  
 Comparison Case: Room Temperature, Blank dia = 54 mm, BHP = 20 bar, Punch Speed = 1 mm/min

Barlat'89 yield criterion covers all the experimental data points. However, Hill'48 is unable to capture yield behavior of Inconel 625 alloy at ND and TD direction. The similar behavior has been seen in case yield stress and anisotropic coefficient variations given in Fig. 18 (b) and (c) respectively. Moreover, similar trend has been seen in all other temperatures and strain rates. Thus, Barlat'89 yielding behavior prediction is more accurate for Inconel 625 alloy.

### Finite element analysis

Numerical simulations of circular deep drawing process have been carried out at different temperatures and BHP with constant punch speed (5 mm/min). Initially, CAD model is developed using Solidworks 14 software and imported in Hypermesh 17 software for meshing. The FEA analysis was done on ABAQUS 6.13 numerical solver package by incorporating subroutine for user defined material (UMAT). Discrete rigid model is used to model punch, die and holder, whose movement is controlled by Rigid body reference node. R3D4 solid element is used for punch, blank holder and die. Blank is modelled as a deformable body and C3D8R solid element with reduced integration is used for the FE analysis. Simulation is carried out for only one quarter axisymmetric model to reduce computational time. Mesh convergence study has been conducted to finalise the optimum element size. In

present study, optimum mesh element size of 1.5 × 1.5 mm<sup>2</sup> with adaptive meshing technique was applied. Finite element analysis was carried on fixed process parameters as mentioned in Table 5. The finite element results of maximum thinning are compared with that of experimental results. The computational time is also an important phenomenon to be considered during fixing the mesh element size. Total 12,896 mesh elements were generated on blank of mesh size 1.5 × 1.5 mm<sup>2</sup>. Various material properties of Inconel 625 alloy calculated in Table 3 were given as an input for blank material. The UMAT code is developed for Sellers constitutive model along with Hill'48 and Barlat'89 anisotropic yield criteria and were used as an input for numerical analysis.

FE simulations were done to verify the experimental results in terms of average thickness, percentage increase in cup height and LDR. The representative measurement for height and thickness of cup is shown in Fig. 19. The experimental and FE simulation comparison for all the experiments is demonstrated in Table 6. The representative comparison of thickness distribution using FE simulations and experimental data at 400 °C, 15 bar BHP and 5 mm/min punch speed is shown in Fig. 20 (a). Barlat'89 yield criterion prediction of thickness distribution shows good relation with experimental thickness distribution. The representative simulated deep drawn cup using Barlat'89 yield criterion at 400 °C temperature, 15 bar BHP and 5 mm/min punch speed and sectional view for

**Fig. 19** Height and thickness measured for cup at 400 °C temperature, 1 mm/min punch speed with 20 bar BHP

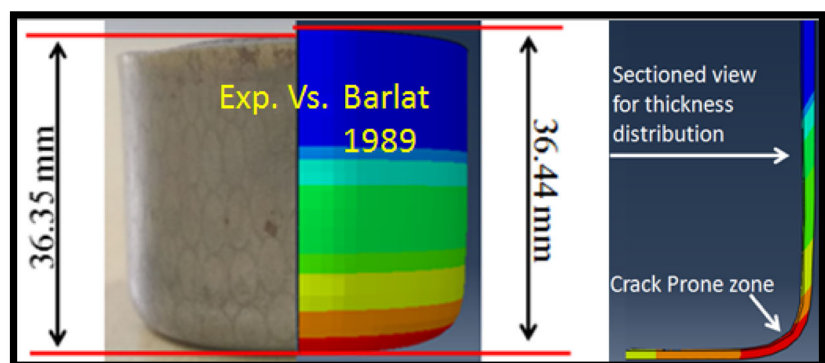




**Table 6** Average thickness and % increase in height in case of Experiment and FEA

Exp. No.	Avg. Thickness Expt. (mm)	Avg. Thickness FEA + Barlat'89 (mm)	Avg. Thickness FEA + Hill'48 (mm)	% Relative Error for thickness (Exp. vs. Barlat'89)	% Relative Error for thickness (Exp. vs. Hill'48)	% Increase in Height of Cup (Exp.)	% Increase in Height of Cup (Barlat'89)	% Increase in Height of Cup (Hill'48)	% Relative Error for height (Exp. vs. Barlat'89)	% Relative Error for height (Exp. vs. Hill'48)
1	0.931	0.926	0.912	0.537	2.041	7.80	7.96	7.88	2.010	1.005
2	0.928	0.887	0.869	4.418	6.358	7.84	7.85	7.89	0.128	0.638
3	0.919	0.886	0.883	3.591	3.917	7.56	7.62	7.76	0.794	2.646
4	0.926	0.915	0.905	1.187	2.267	8.29	8.36	8.39	0.844	1.206
5	0.928	0.892	0.881	3.879	5.065	8.52	8.66	8.70	1.643	2.113
6	0.917	0.911	0.900	0.654	1.854	8.35	8.58	8.64	2.754	3.473
7	0.919	0.906	0.898	1.414	2.285	10.85	10.99	11.26	1.290	3.778
8	0.929	0.899	0.890	3.229	4.198	10.69	10.86	10.82	1.590	1.216
9	0.900	0.886	0.875	1.556	2.778	10.78	10.88	10.97	0.928	1.763
10	0.904	0.896	0.890	0.885	1.548	12.35	12.69	12.75	2.753	3.239
11	0.945	0.934	0.920	1.164	2.646	12.26	12.66	12.69	3.263	3.507
12	0.926	0.936	0.930	1.080	0.432	12.58	12.68	12.72	0.795	1.113
13	0.896	0.891	0.890	0.558	0.696	13.59	13.65	13.76	0.442	1.251
14	0.957	0.944	0.934	1.358	2.403	13.58	13.68	13.74	0.736	1.178
15	0.934	0.937	0.931	0.321	0.321	13.76	13.70	13.72	0.436	0.291

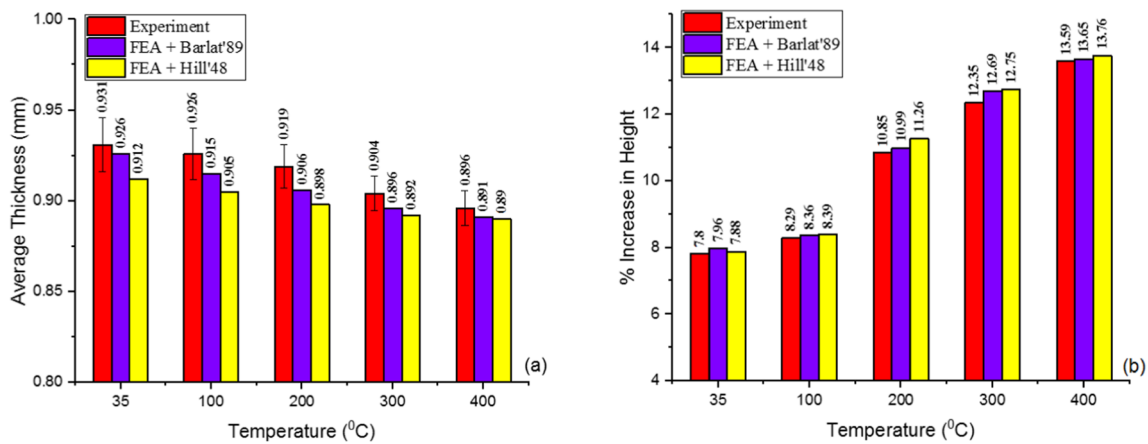


**Fig. 20** Representative comparison of experimental and FE simulation results for (a) average thickness, (b) % increase in height at 400 °C, 15 bar BHP and 5 mm/min Punch Speed

thickness distribution is shown in Fig. 20 (a). Particularly, it predicts thickness value accurately in thinning (punch corner region) and thickening region (top portion of cup wall). The similar trend is observed in all the cases.

To understand the trend of all the performed experiments, average thickness and percentage increase in cup height are measured and demonstrated in Table 6. Sellers constitutive model with Barlat'89 is found to be in good relation with experimental values as the relative error between them for thickness distribution and increase in cup height is well within the 5% of acceptable range. The relative increase in height of drawn cups also increases with temperature as the drawability increases as shown in Fig. 19(b). Barlat'89 criteria more closely followed the experimental results of increase in height of drawn cups as compared to Hill'48 criteria.

## Conclusions

This work involves validation of Seller's model and determining the effect of process parameters over thickness distribution and increase in height of cup. The experimental results are validated with FEA combined with different yield criteria.

Based on the study, following important conclusions can be drawn:

- The material properties, anisotropic parameters and flow stress behaviour are significantly influenced by sheet orientations, strain rates and temperature. As the temperature increases from RT to 400 °C, the reduction in yield strength by approx. 33% (812.07 MPa to 609.5 MPa), ultimate strength by approx. 22.7% (988.55 MPa to 805.18 MPa) and improvement in % elongation from 39% to 47% takes place.
- The Seller's constitutive model displayed good relation with experimental results having correlation coefficient (R) as 0.9721, standard deviation ( $\delta$ ) as 2.314 and avg.

absolute error ( $\Delta$ ) as 5.2616. The relation having combined effect of strain rate and temperature over activation energy was determined. The activation energy was found to be increased with decrease in strain rate and temperature.

- The anisotropic yield behaviour is formulated using Barlat'89 and Hill'48 yield criteria for Inconel 625 alloy. The prediction capability of Barlat'89 in terms of yield locus, anisotropic coefficient variation and yield stress variation is more accurate when compared with Hill'48 yield criterion.
- The LDR increased from 1.8 to 2.13 as the temperature increased from RT to 400 °C. The percentage increase in height was also found to more at higher temperature due to increase in softness of material. FEA of circular deep drawing process was done by incorporation of Sellers constitutive model coupled with Barlat'89 and Hill'48 yield criteria. The Sellers constitutive model with Barlat'89 yield criterion displays good relation for thickness distribution and increase in height of cup with experimental results. All the experiments were having relative error with within 5% of acceptance level for Barlat'89.

Further work involves comparison of various constitutive models with experimental results and determining the earing and other failure defect analysis using experimental and numerical methods.

**Acknowledgements** The author is thankful for the financial aid given by Science and Engineering Research Board (SERB-DST ECR) Government of India (Sanction Number: ECR/2016/001402) and Central Analytical Lab (CAL) of BITS-Pilani, Hyderabad Campus for providing the UTM facility.

## Compliance with ethical standards

**Conflict of interests** The authors declare that they have no conflict of interest.

## References

- Lin YC, Yang H, Xin Y, Li C-Z (2018) Effects of initial microstructures on serrated flow features and fracture mechanisms of a nickel-based superalloy. *Mater Charact* 144:9–21. <https://doi.org/10.1016/j.matchar.2018.06.029>
- Mahalle G, Salunke O, Kotkunde N et al (2019) Neural network modeling for anisotropic mechanical properties and work hardening behavior of Inconel 718 alloy at elevated temperatures. *Journal of Materials Research and Technology* 8(2):2130–2140. <https://doi.org/10.1016/j.jmrt.2019.01.019>
- Shoemaker LE (2005) Alloys 625 and 725: trends in properties and applications. In: *Superalloys 718, 625, 706 and various derivatives* (2005). TMS, pp 409–418
- Jeswiet J, Geiger M, Engel U et al (2008) Metal forming progress since 2000. *CIRP J Manuf Sci Technol* 1(1):2–17. <https://doi.org/10.1016/j.cirpj.2008.06.005>
- Badrish CA, Kotkunde N, Salunke O, et al (2019) Experimental and numerical investigations of Johnson cook constitutive model for hot flow stress prediction of Inconel 625 alloy. In: *Proceedings of the 11th international conference on computer modeling and simulation*. ACM, New York, pp 36–40e
- Cui J, Sun G, Xu J et al (2015) A method to evaluate the formability of high-strength steel in hot stamping. *Mater Des* 77:95–109. <https://doi.org/10.1016/j.matdes.2015.04.009>
- Kardan M, Parvizi A, Askari A (2018) Experimental and finite element results for optimization of punch force and thickness distribution in deep drawing process. *Arab J Sci Eng* 43(3):1165–1175. <https://doi.org/10.1007/s13369-017-2783-9>
- Morchhale A (2017) Study of positioning and dimensional optimization of angled stiffeners using finite element analysis of above ground storage tank. *International Journal of Research in Mechanical Engineering* 10–19
- Wallmeier M, Linvill E, Hauptmann M et al (2015) Explicit FEM analysis of the deep drawing of paperboard. *Mech Mater* 89:202–215. <https://doi.org/10.1016/j.mechmat.2015.06.014>
- Morchhale A (2016) Design and finite element analysis of hydrostatic pressure testing machine used for ductile Iron pipes. *MER* 6(2):23. <https://doi.org/10.5539/mer.v6n2p23>
- Kotkunde N, Deole AD, Gupta AK, Singh SK (2014) Comparative study of constitutive modeling for Ti–6Al–4V alloy at low strain rates and elevated temperatures. *Mater Des* 55:999–1005. <https://doi.org/10.1016/j.matdes.2013.10.089>
- Abedrabbo N, Pourboghrat F, Carsley J (2007) Forming of AA5182-O and AA5754-O at elevated temperatures using coupled thermo-mechanical finite element models. *Int J Plast* 23(5):841–875. <https://doi.org/10.1016/j.ijplas.2006.10.005>
- Naka T, Uemori T, Hino R et al (2008) Effects of strain rate, temperature and sheet thickness on yield locus of AZ31 magnesium alloy sheet. *J Mater Process Technol* 201(1-3):395–400. <https://doi.org/10.1016/j.jmatprotec.2007.11.189>
- Lin YC, Chen X-M (2011) A critical review of experimental results and constitutive descriptions for metals and alloys in hot working. *Mater Des* 32(4):1733–1759. <https://doi.org/10.1016/j.matdes.2010.11.048>
- Lin YC, Li K-K, Li H-B et al (2015) New constitutive model for high-temperature deformation behavior of inconel 718 superalloy. *Mater Des* 74:108–118. <https://doi.org/10.1016/j.matdes.2015.03.001>
- Mahalle G, Kotkunde N, Gupta AK et al (2019) Microstructure characteristics and comparative analysis of constitutive models for flow stress prediction of Inconel 718 alloy. *J of Materi Eng and Perform* 28(6). <https://doi.org/10.1007/s11665-019-04116-w>
- Gujrati R, Gupta C, Jha JS et al (2019) Understanding activation energy of dynamic recrystallization in Inconel 718. *Mater Sci Eng A* 744:638–651. <https://doi.org/10.1016/j.msea.2018.12.008>
- Banabic D (2010) *Sheet metal forming processes: constitutive modelling and numerical simulation*. Springer-Verlag, Berlin Heidelberg
- Kotkunde N, Deole AD, Gupta AK, Singh SK (2014) Experimental and numerical investigation of anisotropic yield criteria for warm deep drawing of Ti–6Al–4V alloy. *Mater Des* 63:336–344. <https://doi.org/10.1016/j.matdes.2014.06.017>
- Barlat F, Brem JC, Yoon JW et al (2003) Plane stress yield function for aluminum alloy sheets—part 1: theory. *Int J Plast* 19(9):1297–1319. [https://doi.org/10.1016/S0749-6419\(02\)00019-0](https://doi.org/10.1016/S0749-6419(02)00019-0)
- Chun BK, Jinn JT, Lee JK (2002) Modeling the Bauschinger effect for sheet metals, part I: theory. *Int J Plast* 18(5-6):571–595. [https://doi.org/10.1016/S0749-6419\(01\)00046-8](https://doi.org/10.1016/S0749-6419(01)00046-8)
- Lin YC, Wen D-X, Chen M-S et al (2016) Improved dislocation density-based models for describing hot deformation behaviors of a Ni-based superalloy. *J Mater Res* 31(16):2415–2429. <https://doi.org/10.1557/jmr.2016.220>
- Naranje V, Kumar S, Kashid S et al (2016) Prediction of life of deep drawing die using artificial neural network. *Advances in Materials and Processing Technologies* 2(1):132–142. <https://doi.org/10.1080/2374068X.2016.1160601>
- Basak S, Panda SK (2017) Implementation of YLD-96 plasticity theory in formability analysis of bi-axial pre-strained steel sheets. *Procedia Engineering* 173:1085–1092. <https://doi.org/10.1016/j.proeng.2016.12.189>
- Prasad KS, Panda SK, Kar SK et al (2018) Effect of solution treatment on deep drawability of IN718 sheets: experimental analysis and metallurgical characterization. *Mater Sci Eng A* 727:97–112. <https://doi.org/10.1016/j.msea.2018.04.110>
- Abedrabbo N, Pourboghrat F, Carsley J (2006) Forming of aluminum alloys at elevated temperatures – part 2: numerical modeling and experimental verification. *Int J Plast* 22(2):342–373. <https://doi.org/10.1016/j.ijplas.2005.03.006>
- Prasad KS, Panda SK, Kar SK et al (2018) Prediction of fracture and deep drawing behavior of solution treated Inconel-718 sheets: numerical modeling and experimental validation. *Mater Sci Eng A* 733:393–407. <https://doi.org/10.1016/j.msea.2018.07.007>
- Kotkunde N, Deole AD, Gupta AK et al (2014) Failure and formability studies in warm deep drawing of Ti–6Al–4V alloy. *Mater Des* 60:540–547. <https://doi.org/10.1016/j.matdes.2014.04.040>
- Verleysen P, Peirs J, Van Slycken J et al (2011) Effect of strain rate on the forming behaviour of sheet metals. *J Mater Process Technol* 211(8):1457–1464. <https://doi.org/10.1016/j.jmatprotec.2011.03.018>
- Lazarescu L, Nicodim I, Banabic D (2015) Evaluation of Drawing Force and Thickness Distribution in the Deep-Drawing Process with Variable Blank-Holding. In: *Key Engineering Materials*. <https://www.scientific.net/KEM.639.33>. Accessed 9 Jun 2019
- Hill R (1990) Constitutive modelling of orthotropic plasticity in sheet metals. *Journal of the Mechanics and Physics of Solids* 38(3):405–417. [https://doi.org/10.1016/0022-5096\(90\)90006-P](https://doi.org/10.1016/0022-5096(90)90006-P)
- Barlat F, Lian K (1989) Plastic behavior and stretchability of sheet metals. Part I: a yield function for orthotropic sheets under plane stress conditions. *Int J Plast* 5(1):51–56. [https://doi.org/10.1016/0749-6419\(89\)90019-3](https://doi.org/10.1016/0749-6419(89)90019-3)

**Publisher's note** Springer Nature remains neutral with regard to jurisdictional claims in published maps and institutional affiliations.